Samuel Hayes[1, 2], Michael Lim[3], Dustin Whalen[4], Paul J. Mann[3], Paul Fraser[4], Roger Penlington[3] and James Martin[3]

[1]MaREI Centre, Beaufort Building, Environmental Research Institute, University College Cork, Ringaskiddy, Cork, Ireland

[2]Department of Geography, University College Cork, Cork, Ireland

[3]Engineering and Environment, Ellison Building, Northumbria University, Newcastle upon Tyne, UK.

[4]Natural Resources Canada, Geological Survey of Canada–Atlantic, Dartmouth, Nova Scotia.

Corresponding author: Samuel Hayes, `shayes@ucc.ie`

Key Points:

- Active headwall properties have a significant effect on headwall retreat rates.
- Passive seismic monitoring is an effective tool for detecting and mapping massive ice surface variability
- Buried massive ice and overburden thickness display variations not predicted from extrapolation of headwall exposures
- Knowledge of inland variations in overburden thickness and massive ice surface elevation reduced the predicted headwall retreat RMSE by 36% compared extrapolation from previous years retreat

Abstract

Retrogressive Thaw Slumps (RTSs), a highly dynamic form of mass wasting, are accelerating geomorphic change across ice-cored permafrost terrain, yet the main controls on their activity are poorly constrained. Questions over the spatial variability of environmentally sensitive buried massive ice (MI) bodies and a paucity of high-spatial and temporal resolution topographic data have limited our ability to project their development and wider impacts. This research addresses these key problems by investigating RTS processes on Peninsula Point — the type site for intra-sedimental MI in the Western Canadian Arctic. Utilizing high-resolution topographic data from drone surveys in 2016, 2017 and 2018 we (1) measure the temporal and spatial variations in headwall properties and retreat rates, (2) determine the spatial pattern of subsurface layering using passive seismic monitoring and (3) combine these to analyse and contextualise the factors controlling headwall retreat rates. We find that headwall properties, namely MI thickness and overburden thickness, are significant controls over rates of headwall retreat. Where persistent ice exposures are present and overburden thickness remains < 4 m, headwall retreat is typically more than double that of other headwalls. Furthermore, a 3D site model was created by combining photogrammetric and passive seismic data, highlighting the variability in internal layering, demonstrating the limitations of extrapolations based

on headwall exposures, and improving predictions of headwall retreat rates compared to long term averages and extrapolations from the previous year. These results provide fresh insights into the controls on headwall retreat rates and new approaches to improve their predictability.

Plain Language Summary

Retrogressive thaw slumps (thaw slumps) are a form of landslide that occurs when thick layers of ice under the ground are exposed and thaw, creating muddy flows that can grow to cover thousands of m^2 in just a few years. These processes are occurring more frequently in the western Canadian Arctic during the last two decades, becoming one of the primary causes of landscape change. This research examines how variation in the ice and overlying soil thickness of the thaw slump headwalls (a prominent, near vertical cliff at the back of a thaw slump), affects their rate of growth. We find that a persistent layer of ice, and a thin soil overburden, tends to promote headwall retreat rates much faster than otherwise. We also show how simple, cost-effective and quick measurements can be used to map the buried ice and show how it varies inland, and then use this information to improve predictions of how fast the headwall will retreat. This research suggests that detailed knowledge of how the internal ice and overburden layering varies is critical to understanding how thaw slumps evolve and to predict their development.

1 Introduction

Unlithified Arctic coastlines are situated on the boundary of three rapidly changing and intertwined systems – terrestrial, oceanic, and atmospheric. Near surface terrestrial permafrost temperatures are increasing (Biskaborn et al., 2019), and active layer depths (ALDs) are growing (Letterly, 2018). Sea ice cover is in a state of rapid decline, and ocean temperatures are increasing (Markus et al., 2009; Steele et al., 2008; Stroeve et al., 2014). Surface air temperatures are warming at an accelerated rate relative to the rest of the planet (Johannessen et al., 2016; Serreze and Francis, 2006). All these changes are expected to continue through the 21st century in response to anthropogenic climate change (AMAP, 2017; Collins et al., 2013; Comiso, 2006). These profound transformations of the Arctic environment are already resulting in significant widespread degradation of coastal permafrost (Fritz et al., 2017; Günther et al., 2013, Günther et al., 2015; Jones et al., 2018; Lewkowicz and Way, 2019; Mars and Houseknecht, 2007; Novikova et al., 2018; Pizhankova et al., 2016; Ramage et al., 2018). One of the most active forms of thermokarst are Retrogressive Thaw Slumps (RTSs), a form of slope failure in which thawed soils and ice melt water flow along a massive ice (MI) body or layer of ice rich permafrost. Active thaw slumps are traditionally characterised by a distinctive "C" shaped scar zone up to 1,000 m wide (Lantuit et al., 2012), containing three main elements (Figure 1);

1. A near vertical headwall consisting of ice poor permafrost and the active layer
2. A steep angled headscarp with exposed ice – the ablation of which drives

the back wasting of the RTS

3. A low angled slump floor, where thawed permafrost material from the headwall combines with meltwater to form a muddy mixture which flows downslope

The areal extent of RTS affected terrain has undergone a dramatic increase in the last two decades across the western Canadian Arctic, where it is now believed to be the dominant driver of geomorphic change in the region (Kokelj et al., 2015; Lantuit et al., 2012; Lewkowicz and Way, 2019; Ramage et al., 2018; Segal et al., 2016). However, attempts to link RTS activity (using metrics such as headwall retreat rates [HWR]) to temperature indices, such as thawing degree days, have proved inconsistent and typically suited to a narrow range of meteorological and geomorphic conditions (Heginbottom, 1984; Jones et al., 2019; Lewkowicz, 1987a; Robinson, 2000, Zwieback et al., 2018). Two key limitations have constrained our understanding of RTS development and evolution, namely: (1) a lack of topographic data with sufficient spatial and temporal resolution and (2) knowledge of subsurface variability in overburden and MI thicknesses.

The recent increase in LiDAR use (Obu et al., 2016; Ramage et al., 2017) and Structure from Motion-Multiview Stereo (SfM-MVS) derived digital elevation models (Cunliffe et al., 2018, Westoby et al., 2012) have provided new opportunities to better constrain topographic controls on RTSs activity. However, detection and mapping of subsurface MI and overburden variability remains primarily limited to visual observations of their exposures along cliffs and headwalls, sporadic borehole measurements and identification of surface features that may act as proxy indicators for the presence of MI. Interpolation and extrapolation of these values to produce regional MI models (Couture and Pollard, 2017; Couture et al., 2018) may result in significant inaccuracies, especially on local scale, placing a limitation of estimates of carbon loss and management of vulnerable infrastructure. Only recently have new methods emerged for mapping massive ice non-invasively using passive seismic recordings (Lim et al., 2020). Here we present a combination of inter-annual, high spatial resolution SfM-MVS data in combination with passive seismic monitoring of subsurface variability to address these critical problems.

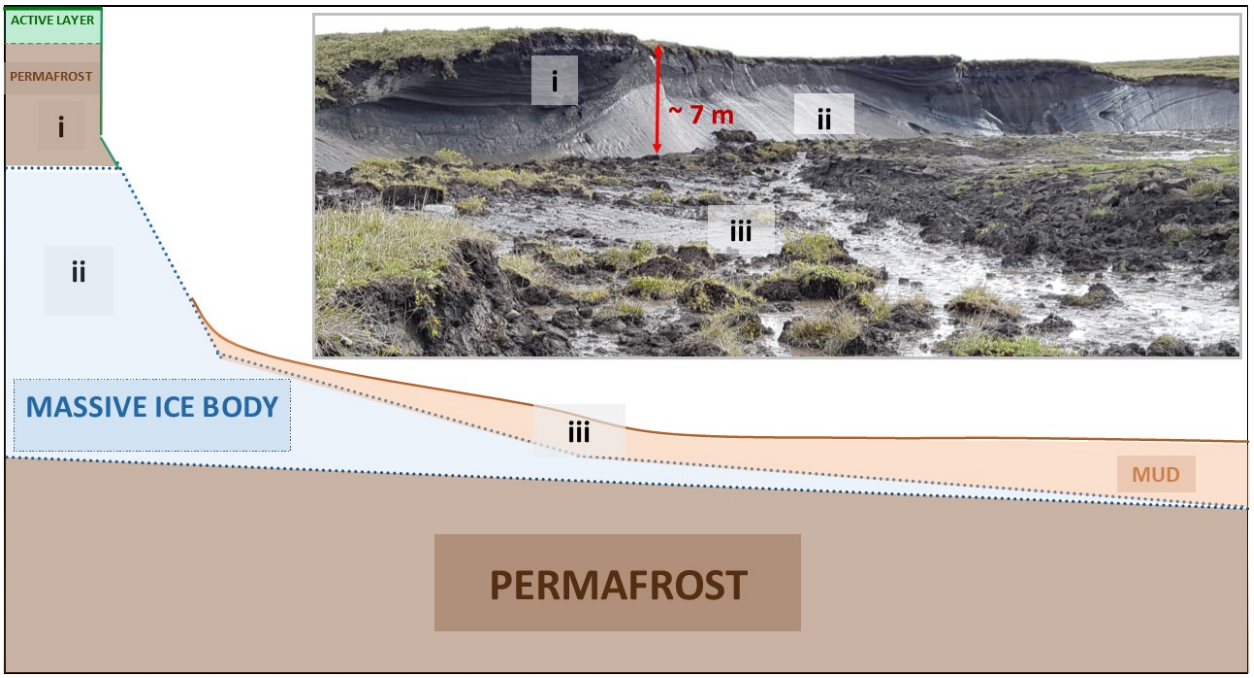

2 Study Area

Peninsula Point is located within the Pingo National Park, 6 km southwest of Tuktoyaktuk, Northwest Territories, Canada (Figure 2). The regional landscape lies within the zone of continuous permafrost, is dominated by rolling hills with a maximum elevation of about 50 m, and thermokarst lake coverage of between 30 and 50 % (Mackay, 1963). Surficial soils consist of various glaciolacustrine and glaciofluvial deposits, a result of its position at the northern edge of the Laurentide ice sheet at the end of the last glacial period (Murton et al., 2005; Mackay, 1971). The climate in the region is considered subarctic, with temperatures below freezing from October to late May, reaching a low of approximately -25 °C between December and March. Temperatures are typically above 0°C from late May to September, coinciding with the period when snow and sea ice cover are largely absent (Burn & Kokelj, 2009). Permafrost in the region is continuous, with temperatures between -6 and -7 °C (Burn & Kokelj, 2009). The Peninsula Point island itself is characterised by a 2 m to 10 m thick layer of clay rich diamicton, atop a MI body of between 5 m and 20 m thickness, some of which lies below sea level. Below the ice lies a layer of deltaic sands (Mackay, 1963). The MI layer is understood to have formed as ground water, sourced from nearby receding glaciers, was forced toward an aggrading permafrost table less than 14,000 years BP (Mackay & Dallimore, 1992; Moorman et al.,1998). Shoreline retreat, MI exposures and RTSs dynamics at Peninsula Point have been monitored since 1935 (Mackay 1986), allowing it to become a "type locality" for massive intra-sedimental ice in the western Canadian Arctic (Murton et

al., 2005). These features make it an ideal site for assessing the role of MI and headwall properties on RTS activity.

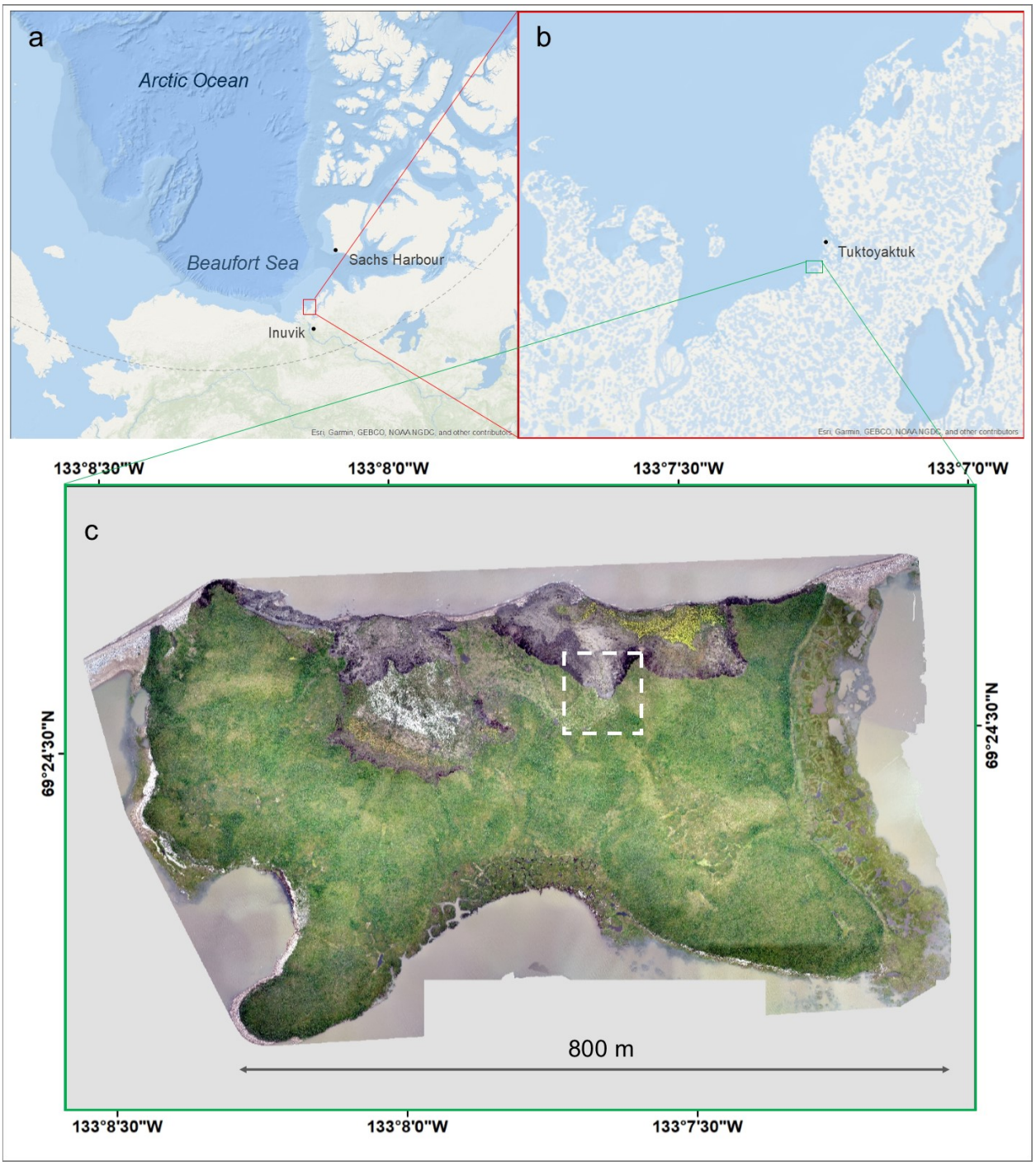

3 Methods and Data

3.1 Remotely Sensed Imagery

High-resolution aerial imagery was captured during the summers of 2016, 2017 and 2018 using the DJI Phantom 4 drone. A total of between 600 and 1000 usable aerial images were collected in each survey. Ten black and white markers were distributed throughout the site to use as ground control points. These were georeferenced using real-time kinematic differential global navigation satellite system to produce centimeter scale locational accuracy. Drone images were processed using the SfM-MVS method to generate high-resolution DEMs and georegistered orthomosaics. SfM-MVS is a photogrammetric range imaging approach that allows for high resolution 2.5D surface reconstruction through the analysis of overlapping 2D images. Images can be captured using consumer grade digital cameras (Carrivick et al., 2016; Westoby et al., 2012), and can produce results with similar levels of accuracy to terrestrial laser scanners, but with a fraction of the cost (James and Robson, 2012; Westoby et al., 2018). The 2016 drone images were processed using Pix4D software. The remaining data were processed using Agisoft Photoscan 1.2.4© (Agisoft, 2016), with all point clouds finely co-registered using the CloudCompare (CC) software (CloudCompare v2.7.0, 2020).

3.1.1 Model Co-Registration

The 2016-point cloud was chosen as the base model on which the other SfM-MVS models were registered, accuracy assessed and rates of HWR determined. Horizontal accuracy was calculated by comparing the position of discreet ground surface features across the three years. For 2017 and 2018, 10 distinct features were used for comparison, resulting in a root mean square error (RMSE) for 2017 of 0.12 m for X, and 0.14 m for Y and an RMSE for 2018 of 0.15 m in X and 0.11 m in Y.

Vertical accuracy was assessed using eight 25 m long elevation profiles in the undisturbed terrain. For 2017 and 2018 the vertical RMSEs were 0.10 m and 0.20 m, respectively.

3.2 Massive Ice Elevation and Overburden Thickness

Determination of the depth to MI followed to process of Lim et al., (2020), but is briefly described here. Seismic noise is present throughout the lithosphere and can be used to gather data on subsurface properties. Monitoring of this noise has been used in various geological settings to determine features such as the depth of subsurface strata or the different seismic wave velocities of the buried rock and soil (Cultrera et al., 2012; Scheib, 2014; Tallett-Williams et al., 2016). Subsurface strata exhibit differences in the amplitude of their vertical and horizontal motions. This occurs due to impedance contrasts between layers and differences in the shear and compressional wave velocities of the materials. This allows for the data to be processed using the H/V (horizonal to vertical) ratio method (Nakamura, 1989) to identify the natural resonance frequencies of the subsurface strata. For a simple two-layer system (in this case the two layers

are overburden and MI), the resonance frequency can be used in the following formula to calculate the depth of the layer boundary:

$$f_r = \frac{V_s}{4h}$$

Where f_r is the resonance frequency, V_s the shear wave velocity and h is the depth.

In August 2017, passive seismic data were collected in nine locations on Peninsula Point, as three separate North to South transects with three measurements each, all using the Tromino® device (http://moho.world/en/tromino/). One transect was along a low-ground segment that had recently been affected by RTS activity and where the active layer extended to the surface of the MI (indicated with "A" label in Figure 3). Two further transects were along undisturbed high ground to both the east and west of the first transect that contained permafrost layers between the ground surface and the MI (indicated with "U" labels in Figure 3). A further five MI height measurements were taken from headwall exposures (indicated with "O" labels in Figure 3).

Processing of the seismic signal allowed for the f_r to be calculated but to determine the depth to the ice it was necessary to calculate the V_s of the overburden layers. This was achieved by selecting two measurement points near the headwall edge, one for the low ground without permafrost and one for the high ground that contained permafrost. The observable depth to ice near these measurement points provided h values, while the H/V processing method provided the f_r values. By using these control measurement points, the V_s for the two overburden layers could then be calculated. For the high ground, this produced a V_s of 1059.38 m s^{-1}, which was then be applied to the five other high ground points to determine their respective depths to the MI surface. For the low ground section, doing the same produced a V_s of 213.8 m s^{-1}, a significantly slower velocity, due to the greater water content of the thawed soil. This value was then applied to the two other low-ground segments to calculate their respective MI depths. Finally, a continuous MI surface layer was then created using the IDW interpolation within ArcGIS 10.3.

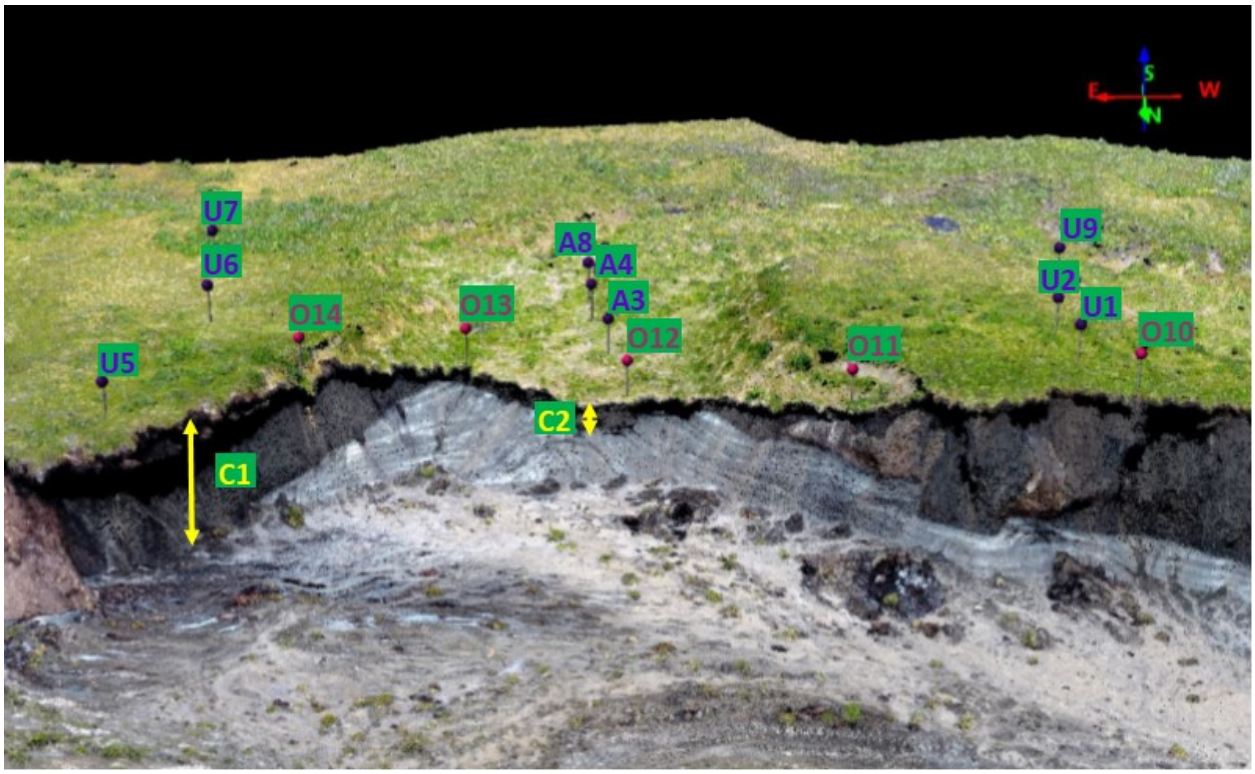

3.3 Active Headwall Properties

Using the SfM-MVS point clouds for 2016, 2017 and 2018, active headwalls were digitized and categorized based on the ice thickness (IT), overburden thickness (OT) and proportion of ice (PI) visible from their exposures. This resulted in three sperate headwall lines in each year, amounting to nine in total. An example of the headwall positions in each year and extra detail of the measurements from a small section is provided in (Figure 4). Transects were added at 5 m intervals, perpendicular to the direction of HWR, where headwall property measurements and retreat rates were measured. Transects that contained no clear exposures of ice in any of the three years were excluded from the numerical analysis and correlations. This reduced the number of usable transects from 163 to 128.

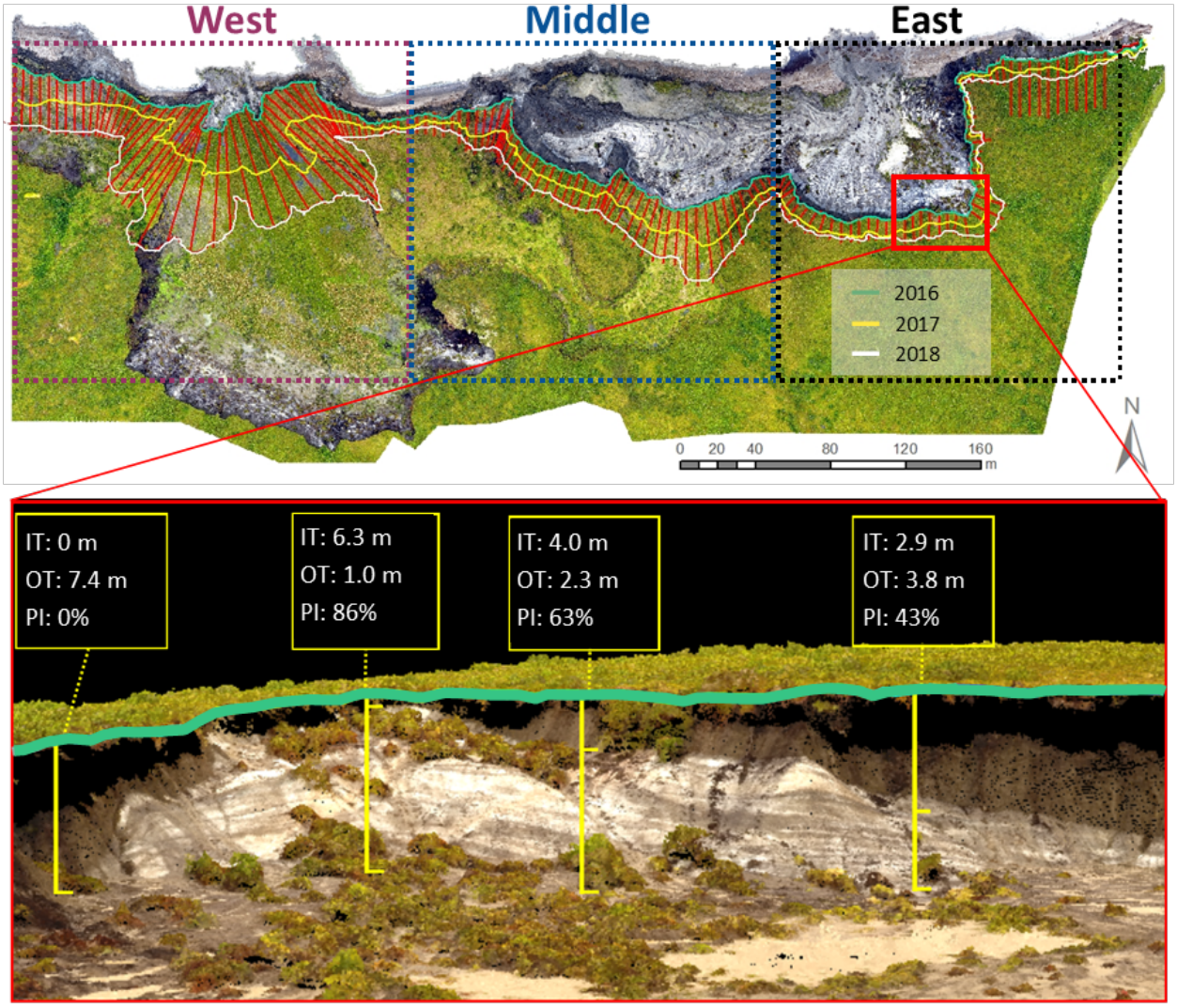

4 Results

4.1 Active Headwall Analysis

4.1.1 Headwall Properties s and Retreat Rate Variations

The average HWR rate increased from 12.5 m from 2016 to 2017, to 13.9 m from 2017 to 2018, with an average of 13.2 m from 2016 to 2018. The east and middle sections (Figure 4) experienced HWR rates of 7.3 m and 11.4 m respectively between 2016 and 2017, reducing to 3.3 m and 9.9 m respectively for 2017 to 2018. In contrast, the west recorded a mean HWR of 16.7 m for 2016 to 2017, increasing to 23.8 m for the 2017 to 2018 period. The HWR rates

over the two years along individual transects ranged from 1.6 m a^{-1} to 41.9 m a^{-1}. Changes in the headwall properties followed a similar pattern to the HWR rates. The IT and PI values decreased overall in the east and middle segments, while increasing in the west. The opposite is true of OT, which increased in the east and middle, and decreased in the west (Table 1).

Table 1:Overall stats in terms of Headwall Retreat (HWR), Ice Thickness (IT) Overburden Thickness (OT) and Proportion of Ice (PI) in headwall exposures on Peninsula Point in 2016, 2017 and 2018. HWR values are for 2016-2017 (2017), 2017 to 2018 (2018) and the 2016-2018 m (note that HWR rates are not available for 2016 as it was the first year of measurement)

	HWR (m)	**IT (m)**	**OT (m)**	**PI**
2016: East	*N/A*	*2.9*	*5.8*	*37%*
2016: Middle	*N/A*	*2.2*	*7.4*	*30%*
2016: West	*N/A*	*0.4*	*2.6*	*15%*
2016: Mean	**N/A**	**1.7**	**5.1**	**26%**
2017: East	*7.3*	*0.5*	*6.6*	*9%*
2017: Middle	*11.4*	*2.4*	*9.3*	*24%*
2017: West	*16.7*	*0.9*	*2.3*	*24%*
2017: Mean	**12.5**	**1.3**	**5.8**	**21%**
2018: East	*3.3*	*0.2*	*6.5*	*5%*
2018: Middle	*9.9*	*0.4*	*9.4*	*9%*
2018: West	*23.8*	*1.7*	*2.2*	*27%*
2018: Mean	**13.9**	**0.9**	**5.7**	**21%**
Mean	**13.2**	**1.3**	**5.5**	**22%**

4.1.2 Ice Thickness and Headwall Retreat

IT values in 2016 and 2017, and the mean IT across all three years, produced weak and variable correlations with HWR rates. However, IT in 2018 produced significant positive correlations with HWR across all timespans, with an overall correlation coefficient of +0.47 between the 2018 IT and the 2016 to 2018 HWR rates ($p < 0.05$). However, no statistically significant differences were noted on the influence of the IT categories in 2018 (no ice, 0-2 m, 2-4 m) on the mean HWR rates (Figure 5a).

In the western section of the headwall the MI was partially covered in 2016 (Figure 6a), but exposure between 2016 and 2017 resulted HWR rates faster than the site average. In combination with the significant relationship between the presence of exposed headwall ice in 2018 and the average HWR rate, this suggests that the presence of MI inland of the headwall, regardless of its absolute thickness, is an important factor controlling HWR rates.

4.1.3 Overburden Thickness and Headwall Retreat

The thickness of the exposed overburden in all years produced statistically significant negative correlations with HWR rates, the strongest being between the average OT across all three years and the average HWR from 2016 to 2018 (-0.52). Examining the mean OT across all three years, the influence over HWR rates can be split into three broad categories; below 2 m, 2 to 4 m and above 4 m. An average OT of 0-2 m produces an average HWR of 27.3 m a^{-1}, 2-4 m OT averages 14.8 m a^{-1}, while all higher categories average between 7.7 and 9.0 m a^{-1} (Figure 5b and Figure 6b). This suggests maintaining an OT of below 4 m tends to produce substantially faster HWR rates than otherwise.

4.1.4 Proportion of Ice and Headwall Retreat

As with the IT, the PI in 2016 had no significant influence over the subsequent HWR rates. Statistically significant correlations were present between the PI in 2017 and HWR rates, but the strongest correlations occurred with the 2018 PI values. The correlation between the 2018 PI and the 2016 to 2018 HWR rate is +0.58 ($p < 0.05$) and with the 2017 to 2018 HWR rate is +0.59. However, as with the IT metric, the correlation is non-linear, influenced heavily by the low HWR associated with the 0% PI category, while any PI above 0%, regardless of their values, are associated with faster rates of HWR. This further supports the idea that the presence of ice inland of the current headwall position, rather than its thickness or headwall proportion, is associated with enhanced rates of HWR (Figure 5c and Figure 6c).

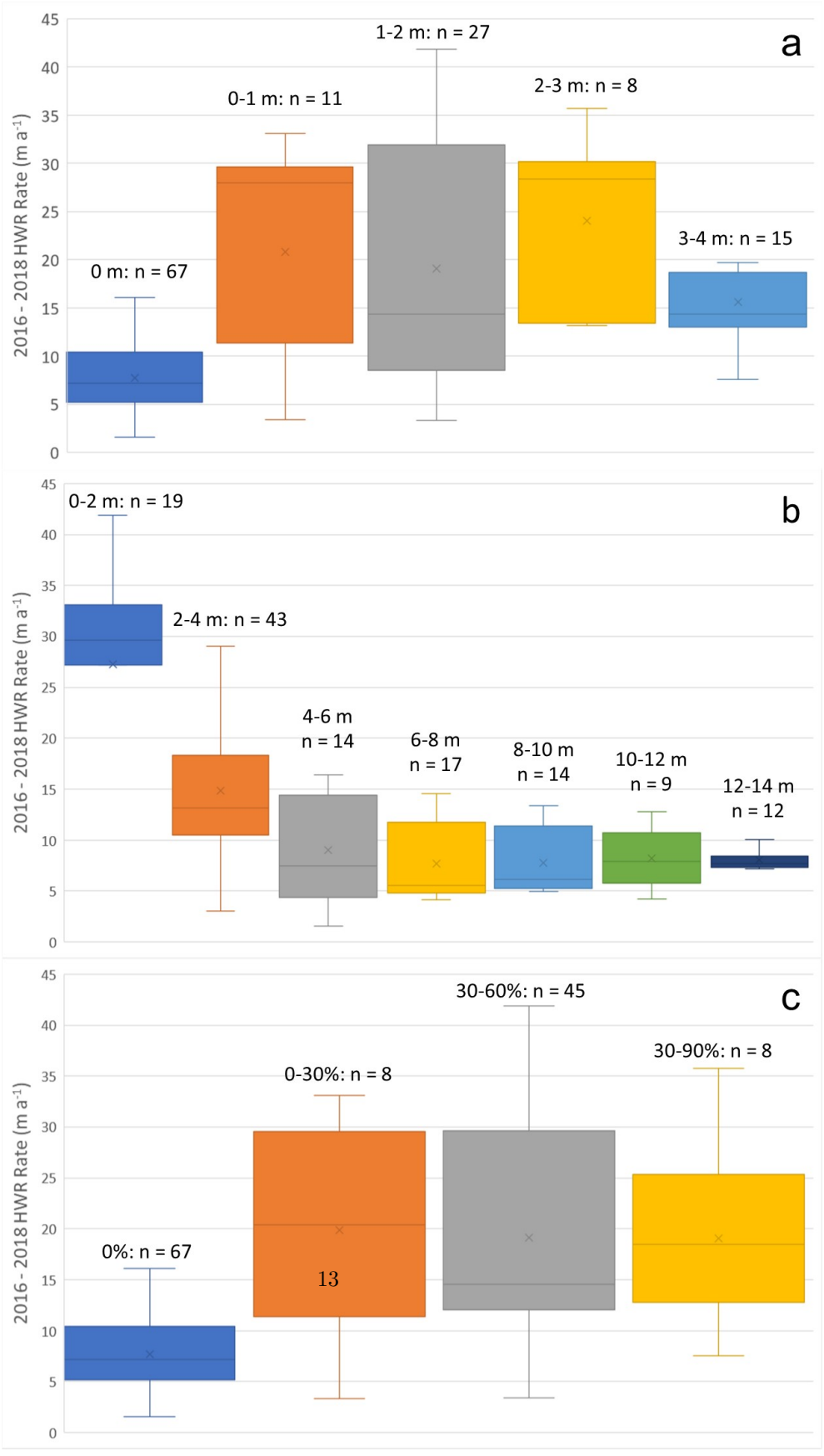
a
2016 - 2018 HWR Rate (m a-1)
0 m: n = 67
0-1 m: n = 11
1-2 m: n = 27
2-3 m: n = 8
3-4 m: n = 15
b
0-2 m: n = 19
2-4 m: n = 43
4-6 m
n = 14
6-8 m
n = 17
8-10 m
n = 14
10-12 m
n = 9
12-14 m
n = 12
c
0%: n = 67
0-30%: n = 8
30-60%: n = 45
30-90%: n = 8

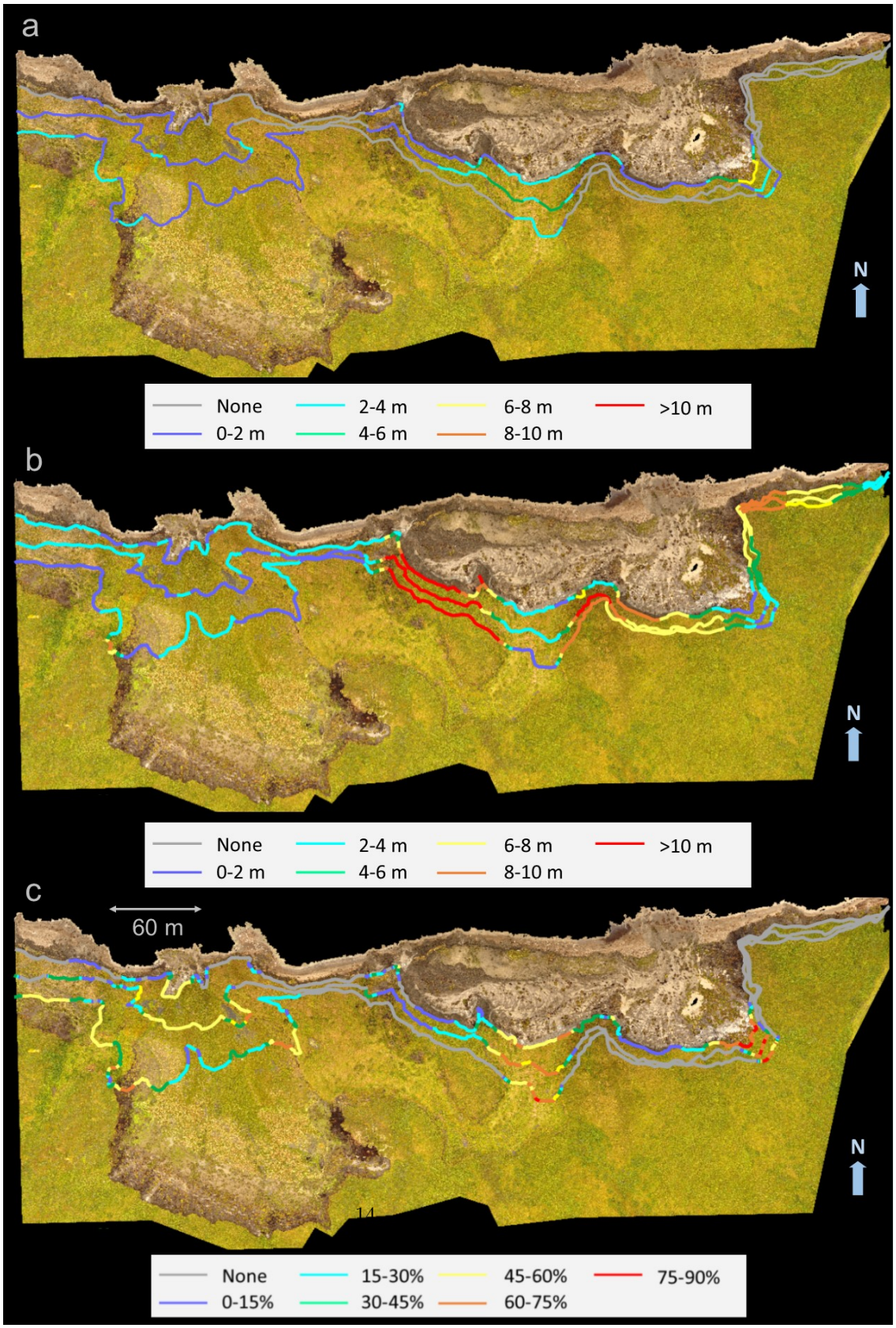
a
N
None
0-2 m
2-4 m
4-6 m
6-8 m
8-10 m
>10 m
b
N
None
0-2 m
2-4 m
4-6 m
6-8 m
8-10 m
>10 m
c
60 m
N
None
0-15%
15-30%
30-45%
45-60%
60-75%
75-90%

4.1.5 *In-situ* Controls on Headwall Retreat Rates

From the analysis thus far, it appears that two factors are the most important in promoting the fastest rates of HWR on Peninsula Point between 2016 and 2018 – a mean OT below 4 m and the presence of ice inland of the headwall, regardless of its thickness or the proportion of the headwall for which it accounted. When both criteria are met, the average HWR rate is 20.4 m a^{-1}, while all other headwalls retreat at an average of 9.5 m a^{-1} (Figure 7).

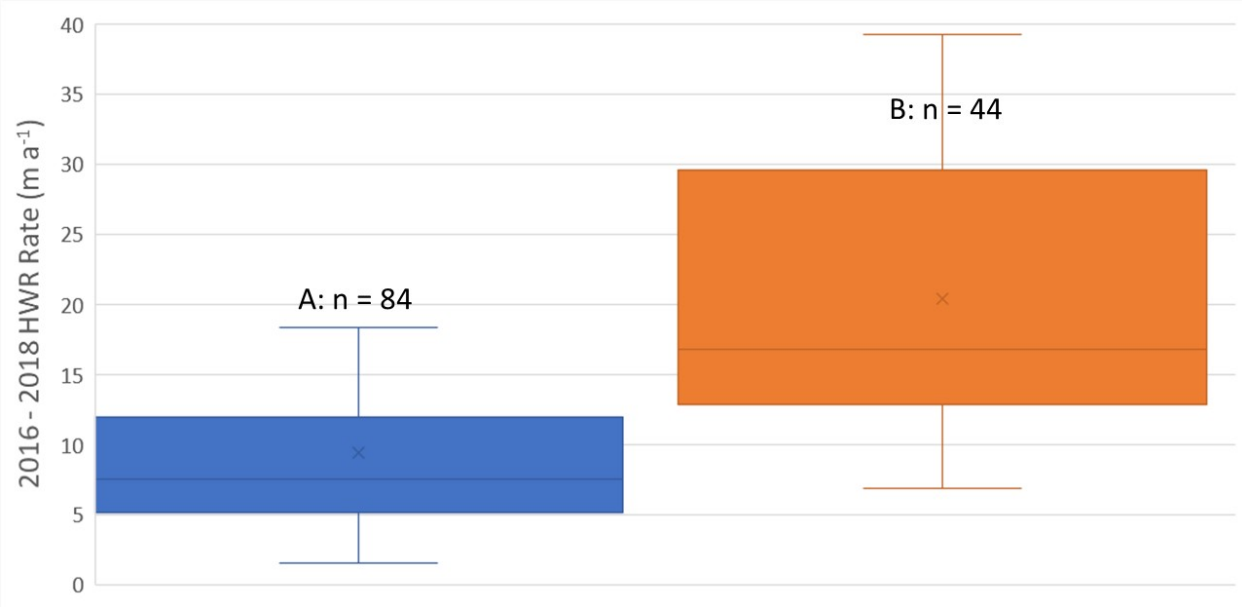

4.2 3D Layer Model

Neither of the two important factors described in the previous section can be determined purely from traditional observational approaches. The presence and surface elevation of buried MI inland of the headwall, and thus the OT also, cannot be determined easily without costly and invasive borehole measurements. Similarly, the presence of water rich active layers, and especially thawed soils reaching the massive ice, attenuate the signals from ground penetrating radar, reducing their effectiveness in these environments (Campbell et al., 2018). Passive seismic measurements now offer the potential to spatially map these changes away from the cliff face and hence produce more accurate forecasts of HWR rates.

Using a combination of the surface elevation data, active layer depth measurements and the MI surface model, a 3D layer model was created for the central portion of Peninsula Point (Figure 8a), allowing for a comparison of surface features with internal OT and MI elevation. A fence diagram was also created to allow for a clearer visualisation of the layers used (Figure 8b-e). The middle portion of the model shows a high elevation ice surface, with a thin overbur-

den and an active layer extending down to the MI, with little change extending inland. The OT averages 2.5 m, with a of 0.6 m (Figure 8b and Figure 8d). The high ground to the east contains an average OT of 9.0 m and a of 1.9 m. The ice and ground surface slowly decrease in elevation inland, resulting in no significant cross-shore trend in OT (Figure 8e). The high ground to the west contains both the most variability in ice surface elevation and OT. The average OT is 10.7 m with a of 2.5 m. It contains a large OT range, from 5.3 m to 14.7 m, and contains a distinct bowl-like depression where the ice surface is close to sea level. These substantial variations in MI elevation are not reflected in the surface topography (Figure 8c).

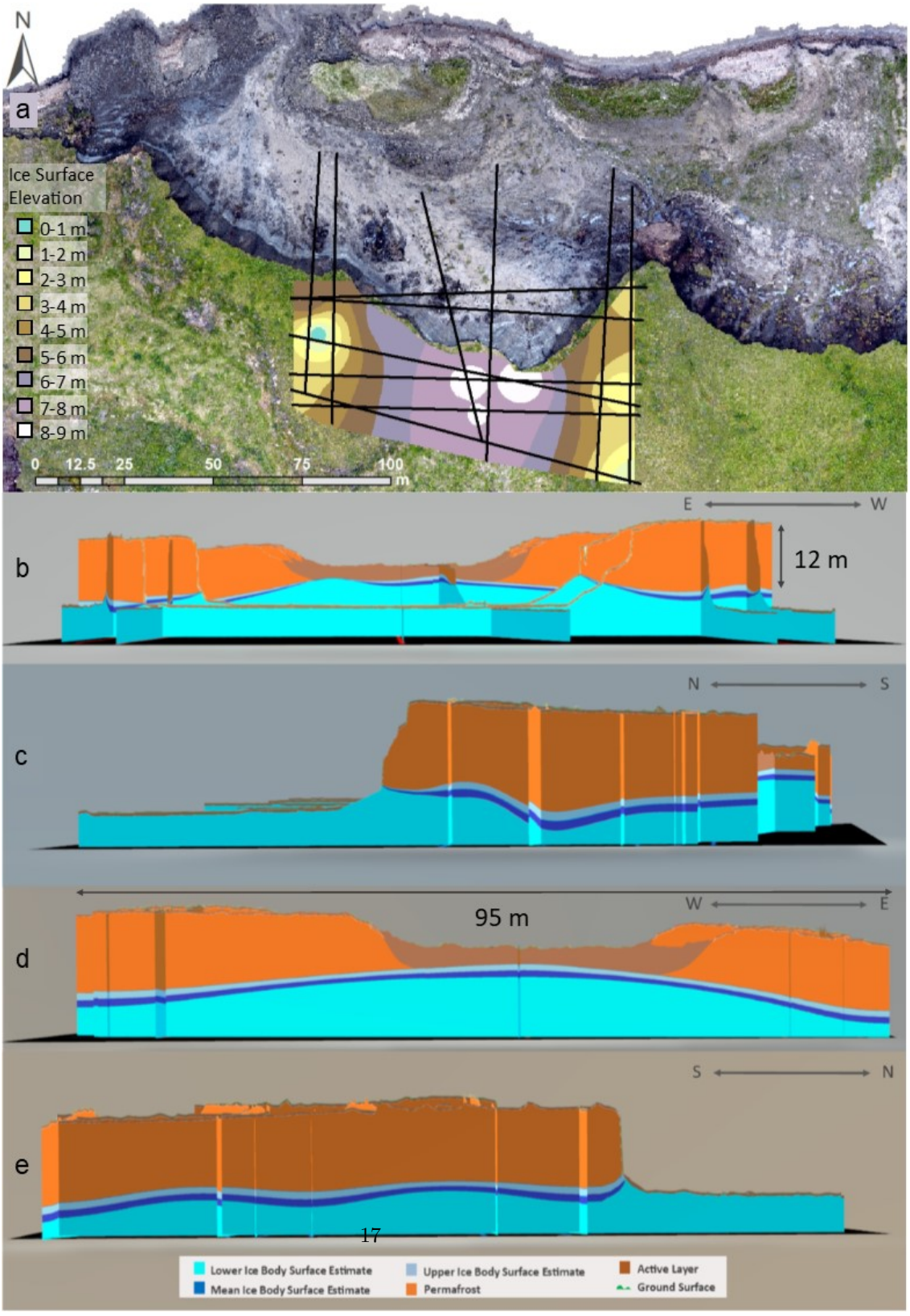
N
a
Ice Surface Elevation
0-1 m
1-2 m
2-3 m
3-4 m
4-5 m
5-6 m
6-7 m
7-8 m
8-9 m
0 12.5 25 50 75 100
m
E W
b
12 m
N S
c
W E
95 m
d
S N
e
Lower Ice Body Surface Estimate
Mean Ice Body Surface Estimate
Upper Ice Body Surface Estimate
Permafrost
Active Layer
Ground Surface

4.2.1 Massive Ice Model Validation

HWR from 2017 to 2018 provides a means of validating the accuracy of the MI model by comparing the modelled ice surface elevation with the resultant 2018 headwall exposures. The trends in IT and OT exposed in the headwalls from 2016 to 2017 can be seen in Figure 9. The IT increased and OT decreased in the middle and western segments, while the opposite trend occurred in the east. The MI elevation model predicts a continuation of a high elevation MI and thin OT in the middle and a reduction in IT and OT in the east. Ice in the west is modelled to dip steeply inland with a large reduction in the PI, counter to the 2016-2017 trend. 2018 in Figure 9 provides a comparison between the predicted MI surface (white dashed line) and the actual MI surface. The model accurately predicted the inland ice surface elevation pattern, with a maximum observed difference of just 1.4 m. The western segment was modelled to dip by between 2° and 18° from the 2017 position but, based on the resultant headwall exposures (and lack thereof), the actual angles are estimated to have been between 10° and 30°. Some ice may have been buried under mud just behind the headwalls and, where the ice is below the base of the headwall, its elevation cannot be determined from visual observations. These factors may have increased the difference in observed and modelled ice elevation.

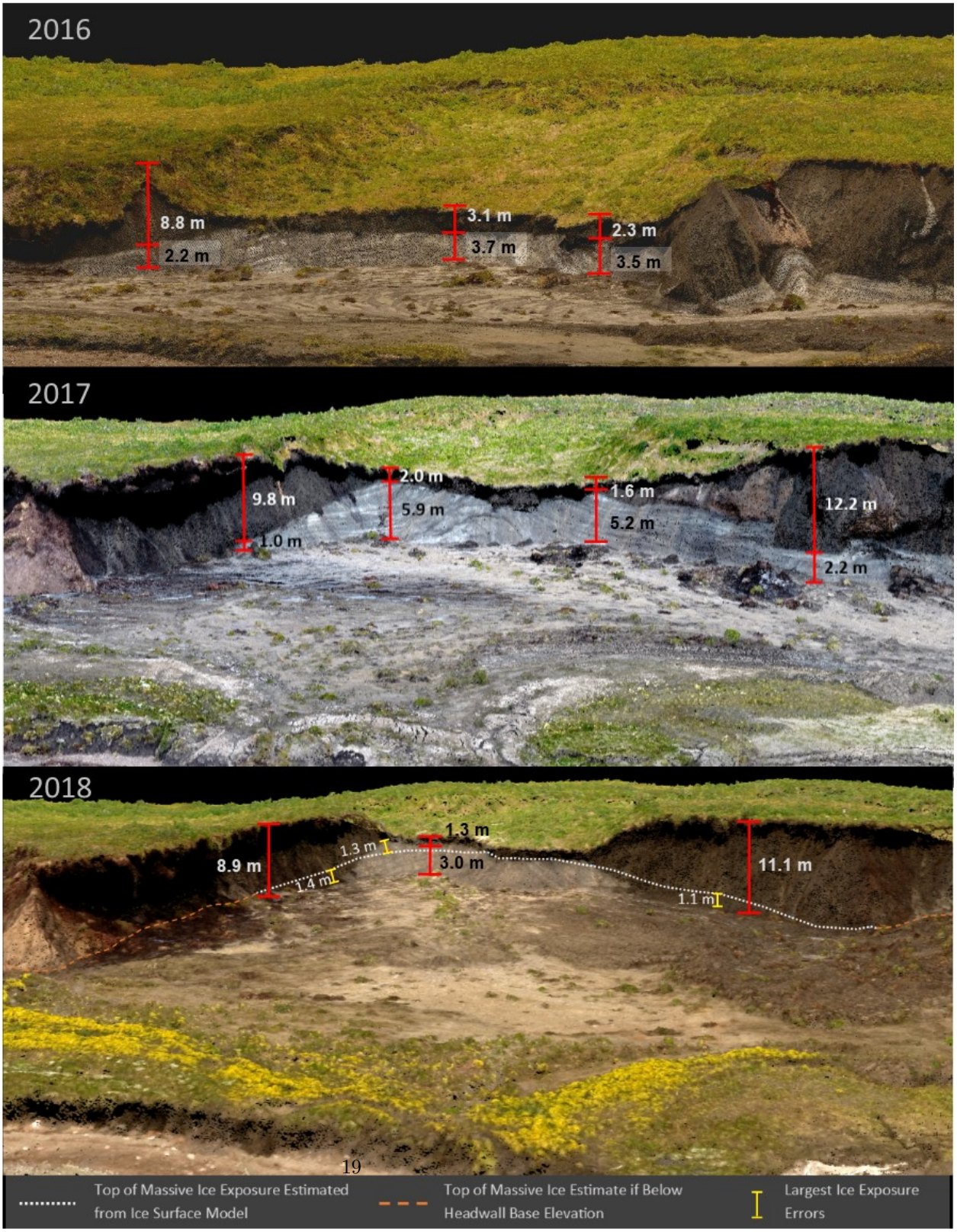
2016
8.8 m
2.2 m
3.1 m
3.7 m
2.3 m
3.5 m
2017
9.8 m
1.0 m
2.0 m
5.9 m
1.6 m
5.2 m
12.2 m
2.2 m
2018
8.9 m
1.4 m
1.3 m
1.3 m
3.0 m
1.1 m
11.1 m
Top of Massive Ice Exposure Estimated from Ice Surface Model
Top of Massive Ice Estimate if Below Headwall Base Elevation
Largest Ice Exposure Errors

4.2.2 Improving HWR Predictions

Our results demonstrate that an OT below 4 m and a consistent exposure of MI within the headwall were the most important factors in producing the fastest rates of HWR at Peninsula Point. A simple index was created to test if accounting for these two *in-situ* controls can improve the prediction of HWR spatial variability across the site. Along the 20 transects that covered the MI surface model, we measured inland from the 2017 headwall position a distance equal to the 2016 to 2017 HWR. The average ice elevation and the average OT along this distance were then given a value based on the criteria in Table 2. These two values were averaged and divided into the 2016 to 2017 HWR distance along each transect to produce a predicted 2017 to 2018 HWR (green line labelled MI). For example, consider a transect that recorded 5 m of retreat between 2016 and 2017, but had no exposed ice and an overburden > 4 m in both 2016 and 2017. If this transect is modelled to have an exposure of ice and an OT < 4 m after 2017, using Table 2, the predicted HWT from 2017 to 2018 would be 6.7 m (5 m divided by 0.75).

These predictions were compared with similar metrics based on the assumption that the headwall properties present in 2017 extended inland (blue line labelled OBS), an extrapolation of the 2016 to 2017 HWR (red line labelled EXT) and with the HWR of 7 m a^{-1} on active retreating headwalls on Peninsula Point as described by Mackay (1986) (pink line labelled MAC), and plotted together in Figure 10.

Table 2: Criteria and values used to create the 2017 to 2018 HWR prediction

Overburden Thickness		**Ice Exposure**	
< 4 m in 2016, > 4 m in 2017 & 2018	**2**	Ice in 2016: no ice in 2017 & 2018	**2**
< 4 m in 2016 & 2017: > 4 m in 2018	**1.5**	Ice in 2016 & 2017: not in 2018	**1.5**
Remains the same	**1**	Remains the same	**1**
> 4 m in 2016 & 2017: < 4 m in 2018	**0.75**	No ice in 2016 & 2017: ice in 2018	**0.75**
> 4 m in 2016: < 4 m in 2017 and 2018	**0.5**	No ice in 2016: ice in 2017 & 2018	**0.5**

Compared to the actual recorded HWR distance across the 20 transects from 2017 to 2018, the RMSE was 6.5 m for MAC, 4.2 m for EXT, 3.3 m for OBS and 2.7 m for MI. The mean absolute errors were 5.3 m, 3.4 m, 2.3 m and 1.8 m, respectively. For MAC only one transect was within 1 m of the actual headwall position in 2018, while eight had errors over 5 m. The same statistics for EXT were five under 1 m and five over 5 m, for OBS there were nine under 1 m and three over 5 m and for MI there were nine under 1 m and one over 5 m.

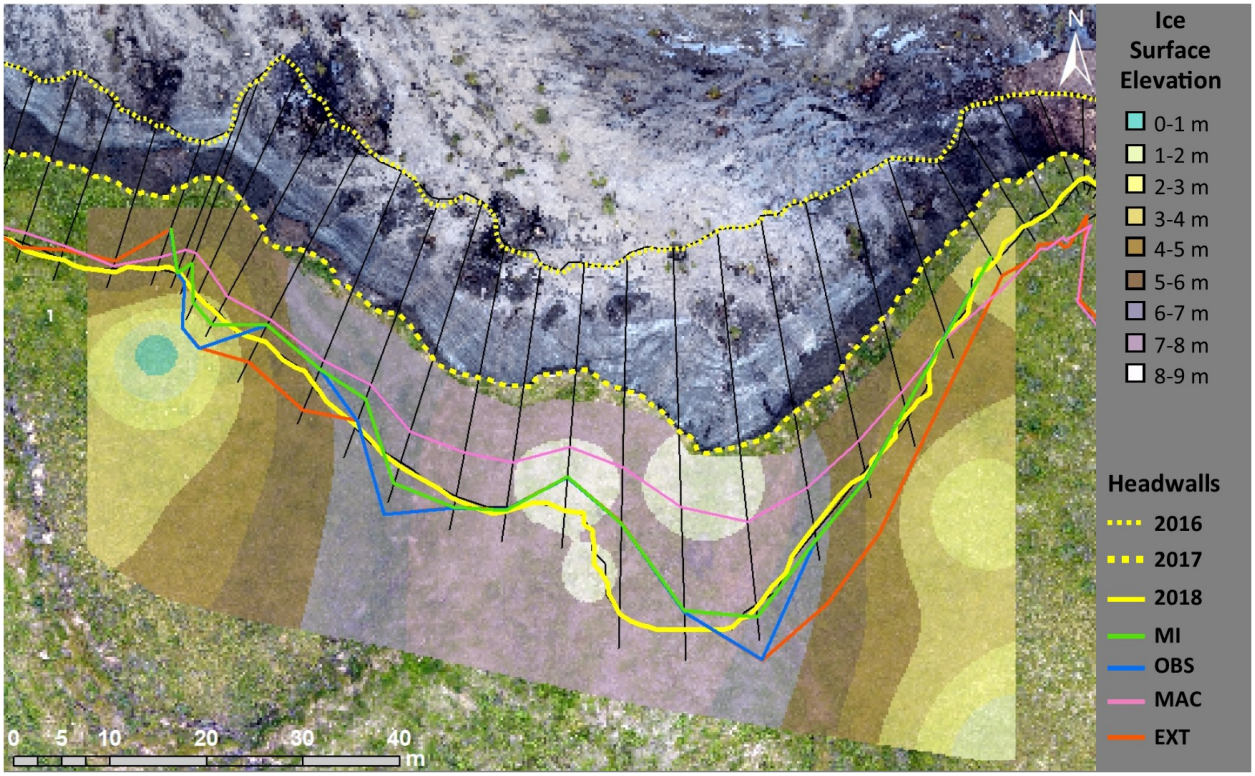

5 Discussion

5.1 Passive Seismic for Subsurface Layer Mapping

The MI surface model was shown to accurately represent the internal surface variations of the MI body and OT, demonstrating the efficacy of the passive seismic device and analysis method presented. The layer model also revealed variability not detectable from headwall exposures, their extrapolations or surface features, such as the rapid reduction in ice surface elevation and the bowl-like depression in the western section. Using the 2018 headwall exposures, a maximum difference of 1.4 m was found between the modelled and observed MI surface. When comparing the headwall exposures closest to the passive seismic measurement points, where the ice surface is not modelled below the headwall base, the layer boundaries were accurate to within 0.5 m. These validations demonstrate that the technique can be used to accurately detect subsurface layering depth and suggest that a greater density of measurements may be required to accurately capture the fine scale variations. Furthermore, knowledge of the MI variability and overburden thickness have been noted as critical to understanding the geomorphic response of Arctic landscapes to climate change and other anthropogenic disturbances (Pollard, 1990; Segal et al., 2016). On Banks Island, observations show that there has been a 60-fold increase in RTS numbers between 1984 and 2015 (Lewkowicz and Way, 2019). It has been suggested that

a thin overburden layer, as little as 1 m in places (Lakeman & England, 2012), is a significant contributor to the observed landscape sensitivity on Banks Island. This thin overburden exacerbates the relatively slow warming trend by allowing the surface energy to more easily reach the near surface MI, thus triggering the formation of new RTSs (Rudy et al., 2017; Segal et al., 2016). This highlights the need for locally detailed maps of overburden and MI thickness variability in vulnerable areas, to aid in determining the likelihood of rapid geomorphic disturbances under continued warming in the near future. Finally, more accurate models of the relative proportions of ice and OT can allow for improved estimates of future soil losses, and thus better constrained predictions of carbon, nutrient and pollutant fluxes. They also have important implications for determining future levels of thaw subsidence, a significant contributor towards the cost of building and infrastructure maintenance across permafrost terrain (Clement, 2013; Couture et al., 2018; Couture and Pollard, 2017; Jones et al., 2008).

5.2 Factors Governing Short-Term HWR Rates

Severalprevious studies have focused on thaw indices and simple geometric models in an attempt to understand the drivers and controls on rates of HWR, but the results have been spatially and temporally inconsistent, with several authors citing a lack of locally accurate data on MI and OT as a significant constraint (Heginbottom, 1984; Jones et al., 2019; Lewkowicz, 1987a; Robinson, 2000, Zwieback et al., 2018). Here, we identify two dominant *in-situ* controls upon HWR, firstly a persistent exposure of MI inland of the current headwall position, regardless of its thickness, and secondly an average OT of under 4 m. Along transects where these criteria were met HWR rates were more than twice as fast as otherwise. It appears that on Peninsula Point the absolute thickness and the proportion of the headwall that consists of ice play little role in determining the HWR rates. Rather, the presence of ice allows for the initiation of HWR, with the resulting rate of retreat being largely dictated by the OT.

By using detailed observations of exposed headwall properties, it has been possible to predict the rate of HWR more accurately than simply extrapolating based on recent or historical averages. The accuracy of these predictions are further improved by incorporating the mapping of MI and OT inland of the headwall, with a reduction in the RMSE of 58% compared to predictions based on historical averages, and 36% compared to predictions based on the HWR rates recorded in the previous year. This is especially important in areas where HWR has not yet been initiated, but where the criteria necessary for HWR to occur can now be identified using passive seismic mapping. For example, in the western portion of Peninsula Point, 16 transects contained no visible exposures of MI in 2016 (Figure 6a). However, 11 of those transects experienced HWR $>$ 10 m between 2016 and 2017, four of which exceeded 20 m. Had passive seismic monitoring been carried out in this region in 2016, it may have been possible to identify the region as having the requisite layering (MI and thin OT) to produce rapid rates of HWR once the MI was exposed. This provides

the potential to better predict and therefore mitigate the dramatic geomorphic changes that occur in ice-cored terrain and highlights the need to detect and map MI variability, not only to improve forecasts of HWR rates, but to identify areas where new RTSs are likely to develop.

6 Conclusion

Passive seismic monitoring has been shown to be an effective tool for detecting OT and MI surface variability. The resulting models showed variations in MI not apparent from headwall exposures or surface topographic features, and the opposite of those inferred from simple extrapolations of headwall exposures.

OT and IT were found to exert a significant control over short term HWR rates from 2016 to 2018. Where the OT remained below 4 m and MI was present inland of the headwalls, HWR rates were more than twice as fast the headwalls with differing properties.

By conducting detailed surveys of headwall properties, it is possible to predict HWR rates more accurately than extrapolating based on past rates alone. Furthermore, by mapping and incorporating OT and MI variations inland of the current headwall position, the errors in HWR predictions can be more than halved compared to predictions based on historical averages, and reduced by more than a third compared to extrapolations from the previous years HWR rates

This research brings into focus the need for accurate data on MI and OT in order to understand the spatial and temporal variability in RTS activity. Better knowledge of MI variability can contribute to improved forecasts of coastal change, such as rates of shoreline retreat and volume loss. These findings have the potential to provide more accurate estimates of nearshore carbon and sediment fluxes and to improve assessments of the susceptibility of local landscapes to rapid geomorphic changes. We emphasise the need for widespread testing of these headwall metrics and passive seismic monitoring ensure their efficacy and robustness across different ice-cored permafrost terrains.

Acknowledgements

The authors would like to thank the members of NRCan who provided invaluable data and assistance in the field. We express our gratitude to the Aurora Research Institute in Inuvik, and the community of Tuktoyaktuk. The research leading to these results has received funding from the European Union's Horizon 2020 project INTERACT, under grant agreement No 730938 and also the NERC Arctic Office, without which this work would not have been possible.

All field and analysis data are available from Zenodo at (https://doi.org/10.5281/zenodo.4770736).

References

Agisoft PhotoScan Professional, Version 1.2.4 (Software). (2016*). Retrieved from http://www.agisoft.com/downloads/installer/

AMAP. (2017). Snow, Water, Ice and Permafrost in the Arctic (SWIPA). *Arctic Monitoring and Assessment Programme (AMAP), Oslo, Norway. xiv* + 269 pp

Biskaborn, B. K., Smith, S. L., Noetzli, J., Matthes, H., Vieira, G., Streletskiy, D. A., ... & Allard, M. (2019). Permafrost is warming at a global scale. *Nature communications*, *10*(1), 264. https://doi.org/10.1038/s41467-018-08240-4

Burn, C. R., & Kokelj, S. V. (2009). The Environment and Permafrost of the Mackenzie Delta Area. *Permafrost and Periglacial Processes*, *12*(January), 53–68. https://doi.org/10.1002/ppp

Campbell, S., Affleck, R. T., & Sinclair, S. (2018). Ground-penetrating radar studies of permafrost, periglacial, and near-surface geology at McMurdo Station, Antarctica. *Cold Regions Science and Technology*, *148*, 38-49.

Carrivick, J. L., Smith, M. W., & Quincey, D. J. (2016). *Structure from Motion in the Geosciences*. John Wiley & Sons.

CloudCompare v2.7.0 (2020). [GPL software]. Retrieved from http://www.cloudcompare.org/

Collins, M., Knutti, R., Arblaster, J., Dufresne, J. L., Fichefet, T., Friedlingstein, P., ... & Shongwe, M. (2013). Long-term climate change: projections, commitments and irreversibility. In *Climate Change 2013-The Physical Science Basis: Contribution of Working Group I to the Fifth Assessment Report of the Intergovernmental Panel on Climate Change* (pp. 1029-1136). Cambridge University Press.

Comiso, J.C., 2006. Arctic warming signals from satellite observations. *Weather*, *61*(3), pp.70-76. https://doi.org/10.1256/wea.222.05

Couture, N. J., & Pollard, W. H. (2017). A Model for Quantifying Ground-Ice Volume, Yukon Coast, Western Arctic Canada. Permafrost and Periglacial Processes, 28(3), 534-542. https://doi.org/10.1002/ppp.1952

Couture, N. J., Irrgang, A., Pollard, W., Lantuit, H., & Fritz, M. (2018). Coastal erosion of permafrost soils along the Yukon Coastal Plain and fluxes of organic carbon to the Canadian Beaufort Sea. Journal of Geophysical Research: Biogeosciences, 123, 406– 422. https://doi.org/10.1002/2017JG004166

Cultrera, M., Antonelli, R., Teza, G., & Castellaro, S. (2012). A new hydrostratigraphic model of Venice area (Italy). *Environmental earth sciences*, *66*(4), 1021-1030. https://doi.org/10.1007/s12665-011-1307-2

Cunliffe, A. M., Tanski, G., Radosavljevic, B., Palmer, W. F., Sachs, T., Lantuit, H., ... & Myers-Smith, I. H. (2019). Rapid retreat of permafrost coastline observed with aerial drone photogrammetry. *The Cryosphere*, *13*(5), 1513-1528. https://doi.org/10.5194/tc-13-1513-2019

Fritz, M., Vonk, J.E. and Lantuit, H., 2017. Collapsing Arctic coastlines. *Nature Climate Change*, *7*(1), pp.6-7. https://doi.org/10.1038/nclimate3188

Günther, F., Overduin, P. P., Sandakov, A. V., Grosse, G., & Grigoriev, M. N. (2013). Short-and long-term thermo-erosion of ice-rich permafrost coasts in the Laptev Sea region. *Biogeosciences*, *10*, 4297-4318. https://doi.org/10.5194/bg-10-4297-2013

Günther, F., Overduin, P. P., Yakshina, I. A., Opel, T., Baranskaya, A. V., & Grigoriev, M. N. (2015). Observing Muostakh disappear: permafrost thaw subsidence and erosion of a ground-ice-rich island in response to arctic summer warming and sea ice reduction. *The Cryosphere*, *9*(1), 151-178. https://doi.org/10.5194/tc-9-151-2015

Heginbottom, J. A. (1984). Continued headwall retreat of a retrogressive thaw flow slide, eastern Melville Island, Northwest Territories. *Geological Survey of Canada, Current Research part B, Paper*, 363-365. https://doi.org/10.4095/119594

James, M. R., & Robson, S. (2012). Straightforward reconstruction of 3D surfaces and topography with a camera: Accuracy and geoscience application. *Journal of Geophysical Research: Earth Surface*, *117*(F3). https://doi.org/10.1029/2011JF002289

Johannessen, O. M., Kuzmina, S. I., Bobylev, L. P., & Miles, M. W. (2016). Surface air temperature variability and trends in the Arctic: new amplification assessment and regionalisation. *Tellus A: Dynamic Meteorology and Oceanography*, *68*(1), 28234. https://doi.org/10.3402/tellusa.v68.28234

Jones, B. M., Farquharson, L. M., Baughman, C. A., Buzard, R. M., Arp, C. D., Grosse, G., ... & Kasper, J. L. (2018). A decade of remotely sensed observations highlight complex processes linked to coastal permafrost bluff erosion in the Arctic. *Environmental Research Letters*, *13*(11), 115001. https://doi.org/10.1088/1748-9326/aae471

Jones, M. K. W., Pollard, W. H., & Jones, B. M. (2019). Rapid initialization of retrogressive thaw slumps in the Canadian high Arctic and their response to climate and terrain factors. Environmental Research Letters, 14(5), 055006. https://doi.org/10.1088/1748-9326/ab12fd

Kokelj, S. V., Tunnicliffe, J., Lacelle, D., Lantz, T. C., Chin, K. S., & Fraser, R. (2015). Increased precipitation drives mega slump development and destabilization of ice-rich permafrost terrain, northwestern Canada. *Global and Planetary Change*, *129*, 56-68. https://doi.org/10.1016/j.gloplacha.2015.02.008

Lakeman, T. R., & England, J. H. (2012). Paleoglaciological insights from the age and morphology of the Jesse moraine belt, western Canadian Arctic. Quaternary Science Reviews, 47,82–100. https://doi.org/10.1016/j.quascirev.2012.04.018

Lantuit, H., Pollard, W. H., Couture, N., Fritz, M., Schirrmeister, L., Meyer, H., & Hubberten, H. W. (2012). Modern and late Holocene retrogressive thaw slump activity on the Yukon coastal plain and Herschel Island, Yukon Territory,

Canada. *Permafrost and Periglacial Processes*, *23*(1), 39-51. https://doi.org/10.1002/ppp.1731

Letterly, A. (2018, December 20). The Recent State of Permafrost, 2017-2018. *Global Cryosphere Watch*. (Accessed 2019, December 1). Retrieved from: https://globalcryospherewatch.org/assessments/permafrost/

Lewkowicz, A. G. (1987a). Headwall retreat of ground-ice slumps, Banks Island, Northwest Territories. *Canadian Journal of Earth Sciences*, *24*(6), 1077-1085. https://doi.org/10.1139/e87-105

Lewkowicz, A. G., & Way, R. G. (2019). Extremes of summer climate trigger thousands of thermokarst landslides in a High Arctic environment. *Nature communications*, *10*(1), 1329. https://doi.org/10.1038/s41467-019-09314-7

Lim, M., D. Whalen, J. Martin, P. J. Mann, S. Hayes, P. Fraser, H. B. Berry, and D. Ouellette (2020). Massive Ice Control on Permafrost Coast Erosion and Sensitivity. *Geophysical Research Letters:* https://doi.org/10.1029/2020GL087917

Mackay, J. R. (1963). *The Mackenzie Delta Area, N.W.T.* Queen's printer. Retrieved from https://books.google.co.uk/books?id=MWfIMgAACAAJ

Mackay, J. R. (1971). *Canadian Journal of Earth Sciences*, *8*(4), 397-422. The origin of massive icy beds in permafrost, western Arctic coast, Canada. https://doi.org/10.1139/e71-043

Mackay, J. R. (1986). Fifty years (1935-1985) of coastal retreat west of Tuktoyaktuk, District of Mackenzie. *Geological Survey of Canada*, 727-735. https://doi.org/10.4095/120445

Mackay, J. R., & Dallimore, S. R. (1992). Massive ice of the Tuktoyaktuk area, western Arctic coast, Canada. *Canadian Journal of Earth Sciences*, *29*(6), 1235–1249. https://doi.org/10.1139/e92-099

Markus, T., Stroeve, J.C. and Miller, J. (2009). Recent changes in Arctic sea ice melt onset, freeze up, and melt season length. *Journal of Geophysical Research: Oceans*, *114*(C12). https://doi.org/10.1029/2009JC005436

Mars, J. C., & Houseknecht, D. W. (2007). Quantitative remote sensing study indicates doubling of coastal erosion rate in past 50 yr along a segment of the Arctic coast of Alaska. *Geology*, *35*(7), 583-586. https://doi.org/10.1130/G23672A.1

Moorman, B. J., Michel, F. A., & Wilson, A. T. (1998, June). The development of tabular massive ground ice at Peninsula Point, NWT, Canada. In *Proceedings of the Seventh International Conference on Permafrost, Lewkowicz AG, Allard M (eds). Collection Nordicanada* (No. 57, pp. 757-762).

Murton, J. B., Whiteman, C. A., Waller, R. I., Pollard, W. H., Clark, I. D., & Dallimore, S. R. (2005). Basal ice facies and supraglacial melt-out till of the

Laurentide Ice Sheet, Tuktoyaktuk Coastlands, western Arctic Canada. *Quaternary Science Reviews*, *24*(5–6), 681–708. https://doi.org/10.1016/j.quascirev.2004.06.008

Nakamura, Y. (1989). A method for dynamic characteristics estimation of subsurface using microtremor on the ground surface. *Railway Technical Research Institute, Quarterly Reports*, *30*(1). https://doi.org/10.1109/IGARSS.2015.7326874

Novikova, A., Belova, N., Baranskaya, A., Aleksyutina, D., Maslakov, A., Zelenin, E., ... & Ogorodov, S. (2018). Dynamics of permafrost coasts of Baydaratskaya Bay (Kara Sea) based on multi-temporal remote sensing data. *Remote Sensing*, *10*(9), 1481. https://doi.org/10.3390/rs10091481

Obu, J., Lantuit, H., Fritz, M., Pollard, W. H., Sachs, T., & Günther, F. (2016). Relation between planimetric and volumetric measurements of permafrost coast erosion: a case study from Herschel Island, western Canadian Arctic. *Polar Research*, *35*(1), 30313. https://doi.org/10.3402/polar.v35.30313

Pizhankova, E. I. (2016). Modern climate change at high latitudes and its influence on the coastal dynamics of the Dmitriy Laptev Strait area. *Earths Cryosphere*, *20*(1), 46-59.

Pollard, W. H. (1990). The nature and origin of ground ice in the Herschel Island area, Yukon Territory. In Proceedings, Fifth Canadian Permafrost Conference, Québec (pp. 23-30)

Ramage, J. L., Irrgang, A. M., Herzschuh, U., Morgenstern, A., Couture, N., & Lantuit, H. (2017). Terrain controls on the occurrence of coastal retrogressive thaw slumps along the Yukon Coast, Canada. *Journal of Geophysical Research: Earth Surface*, *122*(9), 1619-1634. https://doi.org/10.1002/2017JF004231

Ramage, J. L., Irrgang, A. M., Morgenstern, A., & Lantuit, H. (2018). Increasing coastal slump activity impacts the release of sediment and organic carbon into the Arctic Ocean. *Biogeosciences*, *15*(5), 1483-1495. https://doi.org/10.5194/bg-15-1483-2018

Robinson, S.D., 2000: Thaw-slump-derived thermokarst near Hot Weather Creek, Ellesmere Island, Nunavut; in Environmental Response to Climate Change in the Canadian High Arctic, (ed.) M. Garneau and B.T. Alt; *Geological Survey of Canada, Bulletin* 529, p. 335–345

Rudy, A. C. A., Lamoureux, S. F., Kokelj, S. V., Smith, I. R., & England, J. H. (2017). Accelerating Thermokarst Transforms Ice-Cored Terrain Triggering a Downstream Cascade to the Ocean. Geophysical Research Letters, 44(21), 11-080. https://doi.org/10.1002/2017GL074912

Scheib, A. J. (2014). The application of passive seismic to estimate cover thickness in greenfields areas of western Australia—method, data interpretation and recommendations. *Geological Survey of Western Australia, Record*, *201*.

Segal, R. A., Lantz, T. C., & Kokelj, S. V. (2016). Acceleration of thaw slump activity in glaciated landscapes of the Western Canadian Arctic. *Environmental Research Letters*, *11*(3), 034025. https://doi.org/10.1088/1748-9326/11/3/034025

Serreze, M. C., & Francis, J. A. (2006). The arctic amplification debate. *Climatic Change*, *76*(3-4), 241–264. https://doi.org/10.1007/s10584-005-9017-y

Steele, M., Ermold, W., & Zhang, J. (2008). Arctic Ocean surface warming trends over the past 100 years. *Geophysical Research Letters*, *35*(2), 1–6. https://doi.org/10.1029/2007GL031651

Stroeve, J.C., Markus, T., Boisvert, L., Miller, J. and Barrett, A. (2014). Changes in Arctic melt season and implications for sea ice loss. *Geophysical Research Letters*, *41*(4), pp.1216-1225. https://doi.org/10.1002/2013GL058951

Tallett-Williams, S., Gosh, B., Wilkinson, S., Fenton, C., Burton, P., Whitworth, M., ... & Novellis, V. (2016). Site amplification in the Kathmandu Valley during the 2015 M7. 6 Gorkha, Nepal earthquake. Bulletin of Earthquake Engineering, 14(12), 3301-3315. https://doi.org/10.1007/s10518-016-0003-8

Westoby, M. J., Brasington, J., Glasser, N. F., Hambrey, M. J., & Reynolds, J. M. (2012). 'Structure-from-Motion'photogrammetry: A low-cost, effective tool for geoscience applications. *Geomorphology*, *179*, 300-314. https://doi.org/10.1016/j.geomorph.2012.08.021

Westoby, M. J., Lim, M., Hogg, M., Pound, M. J., Dunlop, L., & Woodward, J. (2018). Cost-effective erosion monitoring of coastal cliffs. *Coastal Engineering*, *138*, 152-164. https://doi.org/10.1016/j.coastaleng.2018.04.008

Zwieback, S., Kokelj, S. V., Günther, F., Boike, J., Grosse, G., & Hajnsek, I. (2018). Sub-seasonal thaw slump mass wasting is not consistently energy limited at the landscape scale. *The Cryosphere*, *12*(2), 549-564. https://doi.org/10.3929/ethz-b-000244496